Laser Induced Phased Arrays (LIPA) to detect nested features in additively manufactured components

Don Pieris [a],[*], Theodosia Stratoudaki [b], Yashar Javadi [b], Peter Lukacs [b], Sam Catchpole-Smith [c], Paul D. Wilcox [d], Adam Clare [c], Matt Clark [a]

[a] Department of Electrical and Electronic Engineering, University of Nottingham, UK
[b] Department of Electronic and Electrical Engineering, University of Strathclyde, UK
[c] Department of Mechanical, Materials and Manufacturing Engineering, University of Nottingham, UK
[d] Department of Mechanical Engineering, University of Bristol, UK

HIGHLIGHTS

- Remote, couplant free, non-destructive inspection of an AM component
- Capability to detect cylindrical features as small as 0.2 mm in diameter within AM components with internal roughness
- Noncontact and non-destructive imaging of nested features up to 26 mm deep within AM components

GRAPHICAL ABSTRACT
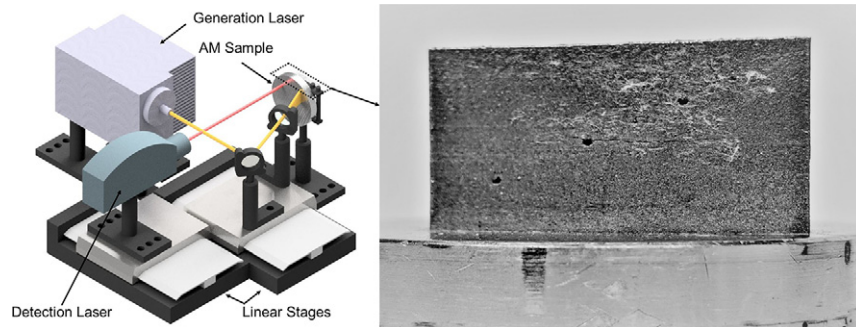
ARTICLE INFO

ABSTRACT

Additive manufacturing (AM) has the capability to build complex parts with internal features, which have many advantages over conventionally manufactured parts. This makes AM an alternative for advanced manufacturing sectors. AM components suffer from defects due to the lack of understanding in the build process. This makes the adaptation of AM in safety-critical industries, such as aerospace, problematic. The current AM work flow calls for costly off-line inspections to qualify components as defect-free. The layer by layer nature of the AM provides an opportunity for an on-line inspection to take place. This can provide early detection of defects as well as information for optimization and repair of the build. Laser Induced Phased Arrays (LIPA) present themselves as a viable remote, non-destructive, ultrasonic technique capable of being implemented as part of an on-line inspection of AM. Lasers are used to generate and detect ultrasound and a phased array is synthesized in post-processing. This paper demonstrates the capability of LIPA to successfully detect and locate features within AM components off-line. Cylindrical features as small as 0.2 mm in diameter and 26 mm above the inspection surface were detected using LIPA and verified using X-ray computed tomography (XCT).

© 2019 The Authors. Published by Elsevier Ltd. This is an open access article under the CC BY license (http://creativecommons.org/licenses/by/4.0/).

1. Introduction

Additive manufacturing (AM) is defined by the American Society for Testing and Materials as a manufacturing process of joining materials to make objects from 3D model data, usually layer upon layer [1]. This process allows the component to be designed with

* Corresponding author.
  E-mail address: don.pieris@nottingham.ac.uk (D. Pieris).

nested features and complex external geometry. The strength, stiffness and density of these parts can be tailored to the application using various infill patterns. AM processes such as powder bed fusion (PBF) have the capability to manufacture components which could not be produced using conventional methods such as milling and casting [2] and in-process repair of defects found on or close to the built surface may be possible [3].

As AM processes mature over time, their uptake in safety critical industries such as aerospace will be limited due to concerns around part integrity. This is due to defects typically found within AM components such as porosity, balling, geometrical defects, surface defects, cracks, delaminations and microstructural inhomogeneities [4,5]. These are caused by a wide range of factors such as the equipment, build parameters and contaminants in the powder feed stock. The on-line detection and classification of such defects can help improve the build process, provide an insight into the components structural capabilities and its service life. Such information can assist a machine user in making an informed decision to either abandon the build or initiate a repair strategy making it more cost effective. Due to the layer by layer nature of the AM process, an on-line inspection can be carried out on an intermediate layer before the build is completed. Consequently, on-line inspection can be used as a part of a feedback loop to optimize build parameters for the current build and any future builds.

On-line process monitoring of AM is currently the topic of intense research and attempts are made by monitoring a variety of parameters. Berumen et al. used a coaxial monitoring system with two sensors to image and measure the surface temperature and temperature distribution of the melt pool [6]. This information was used to understand the melt pool size and shape. As part of a feedback loop, the system was used to improve any sub-optimal build conditions. A similar system was used by Doubenskaia et al. to inspect the heat-affected zone around the melt pool [7]. This combined with the XY position data was used to obtain an understanding of deformations due to thermal stresses and minimize the overheating of overhanging features. Kanko et al. used an Inline Coherent Imaging (ICI) system to investigate the effect that varying process parameters, such as laser power, scan speed and layer thickness would have on the melt pool and the surrounding area morphology during the build [8].

The above mentioned NDE techniques could not image internal features within AM components. The aim of this paper is to utilize the remote and non-destructive nature of Laser Induced Phased Arrays (LIPA) to ultrasonically image nested features within AM components, paving the way for on-line inspection. Unlike other laser ultrasonic techniques, LIPA were previously shown to be capable of non-destructively detecting defects of 1.2 mm diameter, at depths of up to 20 mm away from the inspection surface [9]. As part of this study, a cuboid was manufactured with through holes up to 26 mm deep, with the aim of demonstrating the capability of LIPA to detect features kin to cooling holes embedded within a component manufactured using AM. The sample was then inspected using LIPA and the results were verified using X-ray computed tomography (XCT) and conventional ultrasonic phased array.

1.1. X-ray computed tomography

Currently the only way in which a volumetric inspection could be performed on an AM component would be using XCT post-manufacture. XCT was inherently different to the other NDE techniques as it constructed a 3D figure of the part being inspected using several 2D projections around a central axis [10]. This requirement to obtain multiple projections by manipulating the component or X-ray source and detector, made the implementation of such a system, as part of an on-line inspection for AM, impractical. The high cost of an XCT system on its own was a further barrier. XCT however

has been used extensively in AM for the inspection of powders used, small individual components of about 5 mm and large components of about 100 mm [11]. Kim et al. utilised laser powder bead fusion to manufacture samples with nested spheres ranging from 0.2 mm in diameter to 2 mm in diameter [12]. The 0.2 mm diameter sphere failed to build but the following 0.4, 0.6, 0.8, 1 and 2 mm spheres were successfully manufactured and detected using XCT. When comparing the XCT data to the CAD, it was clear that the smallest sphere of 0.4 mm, had the greatest difference in volume of about 49%. The largest sphere of 2 mm had a difference in volume of 13%. It was shown that most of the geometrical inaccuracy came from the roof sections of the spheres collapsing in on themselves. Mireles et al. used a combination of in-situ infrared thermography and post-manufacture XCT to detect seeded defects ranging from 0.1 mm to 2 mm manufactured using electron beam melting [13]. The results presented illustrate the capability of the in-situ system to detect defects as small as 1.1 mm and how with the use of a remelt strategy can correct the previously detected defects. The XCT and infrared thermography data was used to measure the seeded defects. It was observed that the infrared thermography consistently overestimated the size of the features. Some in situ inspections have been carried out using XCT but within very controlled conditions on single laser scan tracks [14]. Du Plessis et al. discussed a wide range of studies where XCT was used to detect defects several orders of magnitude smaller than that discussed in this study [15]. The literature reviewed above illustrated how XCT was seen to be the gold standard when it comes to post-manufacture analysis of AM components post-manufacture analysis of AM components. This showed that although impractical as an on-line technique, XCT was very useful as a post-manufacture verification tool.

1.2. Ultrasonics

Ultrasonics are typically used to image internal features in optically opaque components. The majority of ultrasonic techniques are based on piezoelectric transducers, which require couplant and contact to a flat surface for an inspection to be carried out. Transducer based ultrasonics have been used in the past for the inspection of AM components. Rieder et al. used an unfocused 10 MHz ultrasonic transducer positioned under the build plate in an attempt to correlate changes in the selective laser melting (SLM) process parameters to bulk material properties [16]. They showed that ultrasound was capable of detecting the presence of a 2 mm diameter sphere embedded within a cylinder of diameter 20 mm and 10 mm tall. This was progressed further by manufacturing a half-cylinder with a radius of 50 mm and width of 30 mm, containing nine internal cylinders, 2 mm, 3 mm and 4 mm in diameter increasing with depth [17]. The first row was positioned along the central radius of the build whilst the other two rows were tilted by $+30°$ and $-30°$. The data obtained using a 5 MHz ultrasonic phased array illustrated clear indications from all nine features in their expected locations, although no information regarding the size of the defects could be obtained. Javadi et al. used transducer based ultrasonic phased arrays of 5 MHz and 10 MHz, in conjunction with the total focusing method (TFM), to inspect wire and arc additive manufacture (WAAM) components, which contained several electrical discharge machining (EDM) holes [18]. They illustrated the capability of this system to detect holes down to 0.5 mm in diameter and up to 45 mm deep.

Although examples discussed above were non-destructive, they required contact to the build plate, meaning they would not be sensitive to complex features that were not directly coupled to the build plate. In addition, access and space requirement of transducer based ultrasonics would not be a viable candidate for a true on-line inspection. Their contact nature and couplant requirements would hinder the build process.

Laser ultrasonics (LU) is a remote and couplant free ultrasonic technique that uses lasers to generate and detect ultrasound, offering the capability to cope with variations in surface temperature, roughness and situations with limited access [19,20]. Due to these characteristics, laser-based NDE techniques have a distinct advantage when being considered for an on-line intermediate layer inspection of AM components. In addition, laser based additive processes such as SLM already have the infrastructure, such as galvo-mirrors, in place to deliver and control the laser beam on the surface of the component being built. Patel et al. used galvo-mirrors in conjunction with their LU system, to inspect the as-deposited surface of an AM component, with the aim of carrying out an inspection on-line [21]. Everton et al. illustrated how time of flight LU could be used to detect fabricated subsurface defects of 600–900 μm but were not fully capable of locating and quantifying them [22]. Lévesque et al. used a similar LU apparatus but in the destructive, ablation regime, on the underside of the sample, to carry out LU B-scans, which were improved using the synthetic aperture focusing technique (SAFT) [23]. The results presented illustrate the capability to detect the top surface of the sample and some embedded defects as small as 0.4 mm in diameter. Smith et al. illustrated how a LU technique known as spatially resolved acoustic spectroscopy (SRAS) can be used to detect changes in SLM process parameters alongside detecting and sizing both surface and subsurface defects with a mean pore diameter of 100 μm [24]. Hirsch et al. also used this system to detect changes to the component micro structure caused by variation in the scan strategy and progressed this work by using the SRAS data to inform repair strategies [25,3].

1.3. Laser phased arrays

LU inspections typically suffer from low signal to noise ratio as they only obtain B-scans and there is no ultrasonic beam forming. One way to significantly improve imaging quality is to make laser phased arrays. Previously this has been carried out using one laser source with multiple optical delays or multiple laser sources [26]. Both methods are prohibitively expensive, hardware demanding and offer a limited number of array elements compared to conventional piezoelectric transducer based phased arrays.

An alternative is to synthesize the array in post-processing which is the basic principle behind LIPA [9]. Previously LIPA has been shown to synthesize arrays with a number of elements comparable to conventional phased arrays, using a simple experimental setup. This was achieved by capturing the full matrix, a data acquisition process where all the generation and detection signal pairs are collected. Following full matrix capture (FMC), a variety of different imaging algorithms and signal processing techniques can be applied on the same data set. Previously, the total focusing method (TFM) has been used with LIPA as an imaging algorithm which is considered as the gold standard in phased array imaging [27]. TFM synthesizes a focus on every point within the image, in post-processing.

LIPA combines the benefits of LU with the improved imaging of phased array algorithms, such as TFM, to provide a remote and non-destructive inspection solution for AM.

2. Methods and materials

This section discusses the FMC data acquisition method, the TFM post-processing algorithm and the experimental setup that was used to synthesize LIPA. Finally the design and manufacture of the sample used for this experiment is discussed.

2.1. Full matrix capture and total focusing method

FMC is a data acquisition method developed for conventional ultrasonic phased arrays. In this method, the signal from each generation and detection element pair is captured to form the full matrix

of $N \times N$, where N is the number of array elements [28]. In order to adapt FMC for LIPA, the phased array of N elements was synthesized by scanning the generation line and detection spot across N number of locations. The acquired signals were then processed using the TFM, where the signals from all elements of the LIPA are summed in order to synthesize a focus at every point in the imaging area [28]. In LU all ultrasonic wave modes are excited simultaneously: shear, longitudinal and surface acoustic waves [29]. The shear wave mode is more efficiently excited in aluminum compared to the longitudinal mode and so it has been chosen to be imaged as part of this experiment [30]. The TFM was originally developed for transducer based phased arrays, which have omnidirectional directivity. However, in LU the directivity and detection sensitivity of the shear wave's ultrasonic component has an angular dependency at the thermoelastic regime: for aluminum, the directivity has been shown to have a maximum at ~30° whilst the sensitivity of the detector to the out-of-plane shear wave component has been shown to have a wider angular spread at an angle of ~36°. Previous work discussed how the TFM algorithm has been adapted to account for this angular dependency by introducing apodization terms [9]. As a result, the intensity of the image, $I(r)$, is given by:

$$I(\mathbf{r}) = \left| \sum_{g=1}^{n} \sum_{d=1}^{n} Z_g(\mathbf{r}) Z_d(\mathbf{r}) s_{gd}(t_{gd}(\mathbf{r})) \right| \quad (1)$$

The double summation is over all combinations of ultrasonic generation (g) and detection (d) positions. The signal $s_{gd}(t)$ is the digitally filtered time-traces of the raw signals collected during the experiment. The time delay term (t_{gd}) is given by:

$$t_{gd} = \frac{d_g(\mathbf{r}) + d_d(\mathbf{r})}{c_T} \quad (2)$$

where $d_g(\mathbf{r})$ and $d_d(\mathbf{r})$ are the distances associated with the generation and detection ray-paths to point $\mathbf{r}$. Z_g and Z_d are apodization coefficients that depend on the directivity and sensitivity patterns of the laser generated and detected ultrasound, as described in [31]. The TFM image was enhanced by normalizing the TFM image with the sensitivity image. The latter describes the amplitude expected from a perfect point target (i.e. scattering matrix equal to unity) as a function of position (Fig. 6). The normalized image has uniform sensitivity but non-uniform noise, as opposed to the initial TFM image which has uniform noise but non-uniform sensitivity [9]. These normalized TFM images are used in the work presented in this paper.

2.2. Experimental setup

An IR laser was focused as a line source onto the under side of the sample, as illustrated in Fig. 1. The absorbed laser energy rapidly heated the surface of the sample within its non-destructive, thermoelastic regime, generating ultrasonic waves. The generation laser used was a pulsed neodymium-doped yttrium aluminum garnet (ND:YAG) laser, at an optical wavelength of 1064 nm, a repetition rate of 5 kHz and pulse energy of 0.1 mJ. This was focused down to a line of 5 mm in height and 0.2 mm wide, at incidence angle of ~20° normal to the surface of the sample. The pulse duration of the laser was 1 ns. The pulse length of the laser and short optical absorption depth in aluminum meant that the laser excitation was broadband, up to 400 MHz [29]. A Polytech laser vibrometer was used to measure the out-of-plane displacement of the sample surface, caused by the ultrasonic wave. The vibrometer uses a continuous wave laser, emitting at 633 nm, with power of less than 1 mW, focused down to a 0.04 mm diameter spot, aligned to the center of the generation line source and normal to the surface (Fig. 1). The signal was averaged 500 times to increase the signal to noise ratio (SNR) due to the limited power of
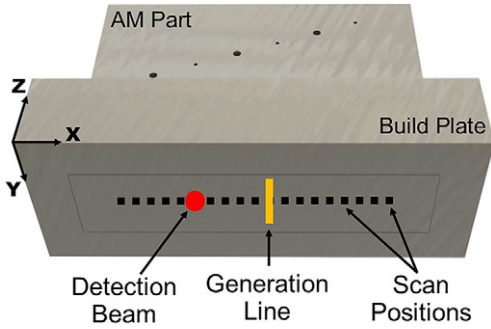
Fig. 1. Schematic view of the under side of the AM sample. The ultrasonic waves were generated using an IR laser focused on to the sample as a line source and detected using a red detection laser focused to a spot 0.04 mm diameter. The under side of the sample was polished in order to maximize the laser detection and is shown here, illustrating all possible positions of the generation line source and detection spot.
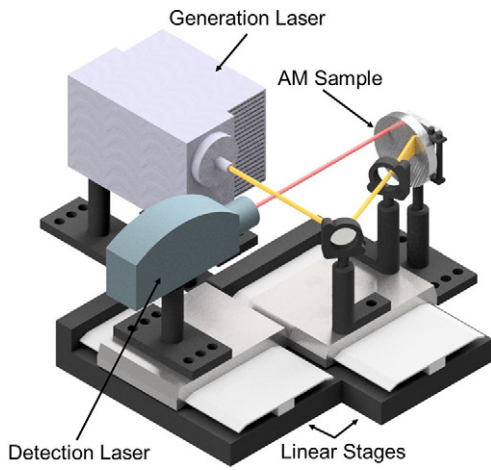

Fig. 2. Experimental schematic illustrating the 1064 nm pulsed generation laser, 633 nm continuous wave detection laser (Polytech vibrometer), the under side of the AM sample and linear scanning stages used to independently move both the generation and detection lasers.

the detection laser. The detector had an upper bandwidth limit of 24 MHz, which set the limit for the ultrasonic frequency of the captured signals.

A 1-D LIPA of 129 elements was synthesized, with an element spacing of 194 μm. The element spacing was chosen to be half the wavelength of the shear wave at 8 MHz in aluminum[1], in order to avoid grating lobe artifacts in the ultrasonic images, up to 8 MHz [33].

As illustrated in Fig. 2, the sample was stationary throughout the experiment whilst the generation and detection lasers were scanned in turns. Once a row of signals where the position of the generation laser was varied, were collected, the detection laser incremented by the width of an element. This process was repeated for 129 elements to build up the 129 × 129 matrix required for FMC.

2.3. Sample design and manufacture

The primary aim when designing the sample was to create internal features that contain typical PBF characteristics such as internal surface roughness and backfilling. Through holes were chosen here
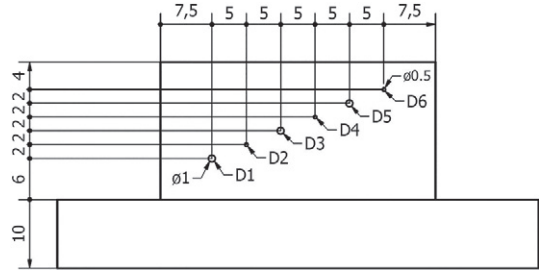

Fig. 3. Side elevation of rectangular cuboid sample built using AM on top of a standard 10 mm Realizer build plate. Six through holes were included in the design and manufactured in to the sample. The hole diameters were alternated between 0.5 mm and 1 mm.

to allow any unfused powder to drain out, as air-filled defects would provide better ultrasonic contrast than powder-filled cavities. In addition, the shape of the defects provided the best case for demonstrating the potential of the ultrasonic method used for defect detection, given that a 1-D LIPA was synthesized. This type of array can provide 2-D, cross-sectional ultrasonic images of the component and the cylindrical shape would provide the best conditions for detection. The uniform cross-section across the width would give a clear indication of the location features in the XZ plane with very little influence from the Y position. The features were sized to replicate internal features kin to cooling holes manufactured using processes such as SLM [34].

The sample was manufactured using a Realizer SLM50 equipped with a 100 W continuous wave laser with a wavelength of 1064 nm. The laser was used to melt and fuse AlSi10Mg powder (TLS Technik) layer-by-layer to build the sample on top of a 10 mm thick aluminum alloy build plate. Throughout manufacture, the build chamber was purged and continuously flushed with argon to ensure a working atmosphere of less than 500 ppm of O_2. The build plate was heated and maintained at 200 ° C, a commonly used technique to reduce the build-up of thermal stresses during manufacture. A pre-sinter scan strategy was used to maximize the bulk density of the material, as described by Aboulkhair et al. [35]. The AM sample was designed to be 20 mm × 40 mm × 10 mm, as seen in Fig. 3. The design included six through holes. The first through hole (D1) was placed 16 mm from the under side of the build plate and the following holes (D2, D3, D4, D5, D6) were placed at depth increments of 2 mm. They were spaced horizontally by equal increments of 5 mm in order to avoid ultrasonic shadowing from the holes below. The through holes were alternately designed to be 0.5 mm and 1 mm in diameter. The manufactured sample seen in Fig. 4 was inspected using XCT and it was found that the holes designed to be 0.5 mm and 1 mm were respectively measured to have a mean diameter 0.2 mm and 0.7 mm (see
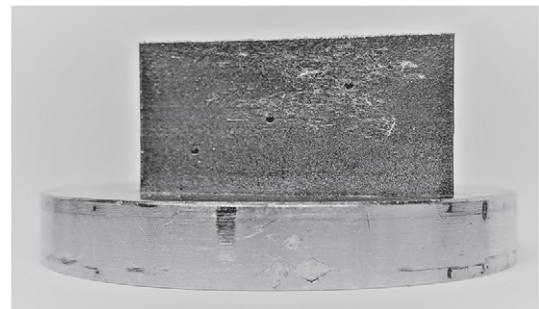

Fig. 4. Side profile of the manufactured sample where the 1 mm through holes are clearly visible compared to the 0.5 mm holes which show some back filling.

---

[1] $\lambda = c_T/f$, where λ is the ultrasonic wavelength, f is the ultrasonic frequency and c_T is the shear wave velocity in aluminum; for $c_T = 3100$ m s^{-1} [32] and $f = 8$ MHz, $\lambda = 194$μm.

Section 4.1). The XCT data in Fig. 7 also revealed the internal roughness found within the through holes consistent with the side profile seen in Fig. 4.

The LIPA were synthesized on the underside of the build plate which was polished down to a finish of 0.05 µm Ra. This was necessary to increase the optical reflection of the detection laser. It is noted here that polishing would not be required if another type of laser detection system was used (e.g. a rough surface interferometer [36,37]).

3. Results

Fig. 5 shows the normalized TFM image using shear-shear wave arrivals based on signals captured using FMC, off the under side of the sample. The data acquisition system used a 1 MHz high pass filter to remove any low frequency noise. Prior to the application of the TFM imaging algorithm, a digital band-pass filter was applied in the frequency domain in order to maximize the SNR and for the case shown in Fig. 5, a band-pass filter centered at 3 MHz with 100% bandwidth, at −40 dB was used.

Laser ultrasound simultaneously excites bulk and surface acoustic waves which means that there is a cross talk region where signals from the surface acoustic waves appears as signals from the shear wave. The extent of the region depends on the array aperture and the velocities of the two ultrasonic waves [9]. It can be seen in Fig. 5 that the affected region extends to ~5 mm from the underside of the sample, which was still within the thickness of the build plate, where no features were present.
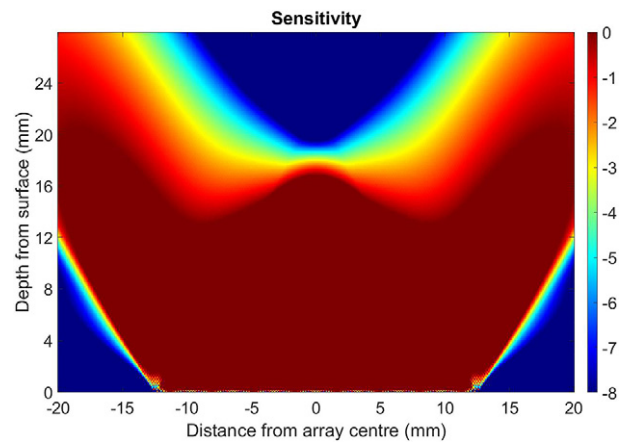

Fig. 6. Sensitivity image for shear-shear waves showing the amplitude expected from a perfect point target as a function of position based on theory [9].

The normalized TFM image shown in Fig. 5 has uniform sensitivity and non-uniform noise: the noise in areas with low sensitivity is amplified. Fig. 6 shows the sensitivity image for shear-shear wave amplitude, expected from a perfect point target as a function of position, based on theory. It illustrates that the top region above the center of the array has low sensitivity (a blind spot), which is due to the angular dependence of the laser-generated and detected shear waves around 0° [31]. This explains noise artifacts seen in the center top section of Fig. 5. It also explains why features D4 and D5 have
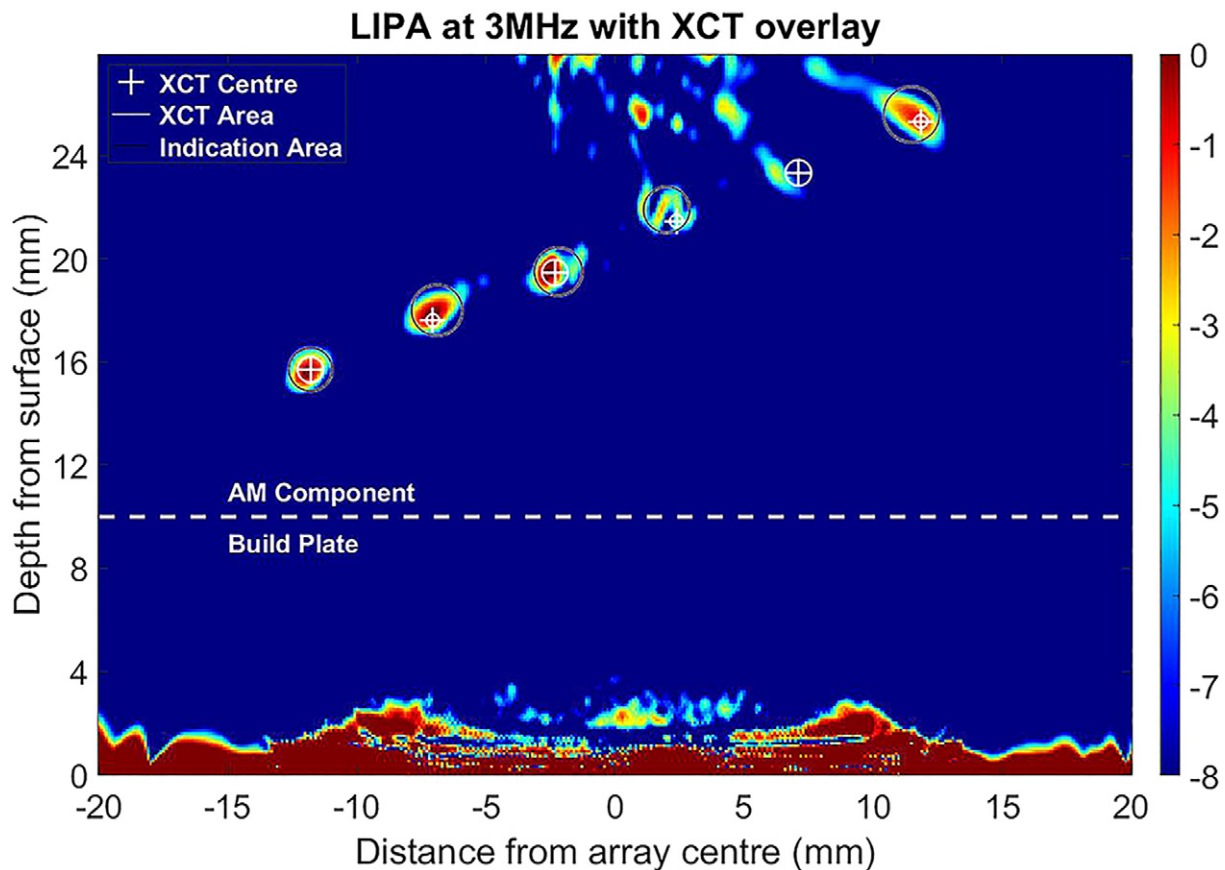

Fig. 5. Normalized TFM image using shear-shear wave arrival. Black circles mark the center of the indications and are proportional to the area. White cross hairs mark the centers located using XCT and white circles represent the area based on the XCT measured diameter. The white dashed line illustrates the separation between the build plate and the part built on top of it.

reduced ultrasonic signal compared to the others, as they are found in this region of low sensitivity.

Five of the six manufactured features are detected in Fig. 5, with the first one (D1) observed at 16 mm from the bottom of the build plate and −13 mm from the middle of the array. The next four features are observed at increasing depths and at an equal horizontal spacing. D5 is not identified due to it appearing just above the noise level. It is 0.7 mm in diameter, located 24 mm from the bottom of the build plate and 7 mm from the center of the array.

4. Discussion

This section discusses how information from XCT and ultrasonic phased arrays were used to verify the built component versus its design. The size and location of the features were extracted from the XCT and used to asses the capability of LIPA.

4.1. Verification

XCT data obtained at a voxel size of 30 μm was used to size the manufactured holes. A best fit cylinder was placed inside each of the holes, the X, Z position and the diameter of these cylinders was extracted and used. This showed that holes designed with a diameter of 1 mm and 0.5 mm were measured to have a mean diameter of 0.7 mm and 0.2 mm. It also showed that the 0.7 mm diameter holes were clear all the way through the cuboid, and the 0.2 mm diameter holes exhibited some back filling, as illustrated in Fig. 7. These small particles present inside the 0.2 mm holes seem to acoustically couple the inner walls of the hole. This, combined with the internal roughness seen in Fig. 7, could explain some loss of ultrasonic signal from the features, such as D6 and D4, due to acoustic scattering. Fig. 7 also shows the horizontal cross-section of D5 which, although it was 0.7 mm in diameter, its ultrasonic signal was just above the noise level, as shown in Fig. 5. It is noted that significant internal roughness is observed in Fig. 7 for this feature which has contributed to the loss of signal. Since D6 and D4 are of similar size and internal structure and
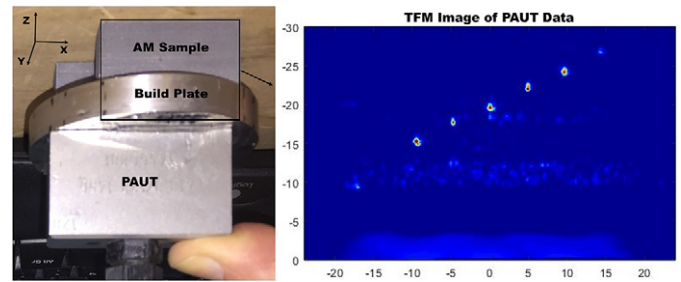

Fig. 8. Experimental setup of phased array ultrasonic probe placed on the underside of the build plate (left). TFM data from the AM sample clearly illustrating all six through holes with a lower intensity indication form the furthest away feature at 26 mm (right).

the same is true for D5 and D3, it is an indication that the low sensitivity of the shear wave in the region where D4 and D5 are located, is more significant reason for the low ultrasonic signal observed in Fig. 5 than the internal roughness and backfilling of these features.

In addition to the XCT analysis, the sample was inspected using a transducer based 10 MHz, longitudinal wave, ultrasonic phased array. The 128 element phased array probe was in direct contact with the under side of the build plate using liquid couplant, as illustrated in Fig. 8. A FIToolbox (Diagnostic Sonar, UK) was employed as the phased array controller which used a real-time TFM software, called CUE-TFM [38]. This generated the TFM image of longitudinal-longitudinal wave arrival, illustrated in Fig. 8 (longitudinal wave velocity in aluminum, c_L = 6400 and ultrasonic wavelength at 10 MHz $\lambda_L \sim 0.64$ mm) [32]. It is worth noting that aside from the six expected indications, some micro-porosity was detected about 10 mm from the bottom of the build plate. This was the region between the cuboid and the build plate, where typically micro-porosity was expected due to the steep thermal gradients during the AM build process. XCT verified the presence of a layer of pores <100 μm in diameter, which is a good observation but outside the scope of the present paper.
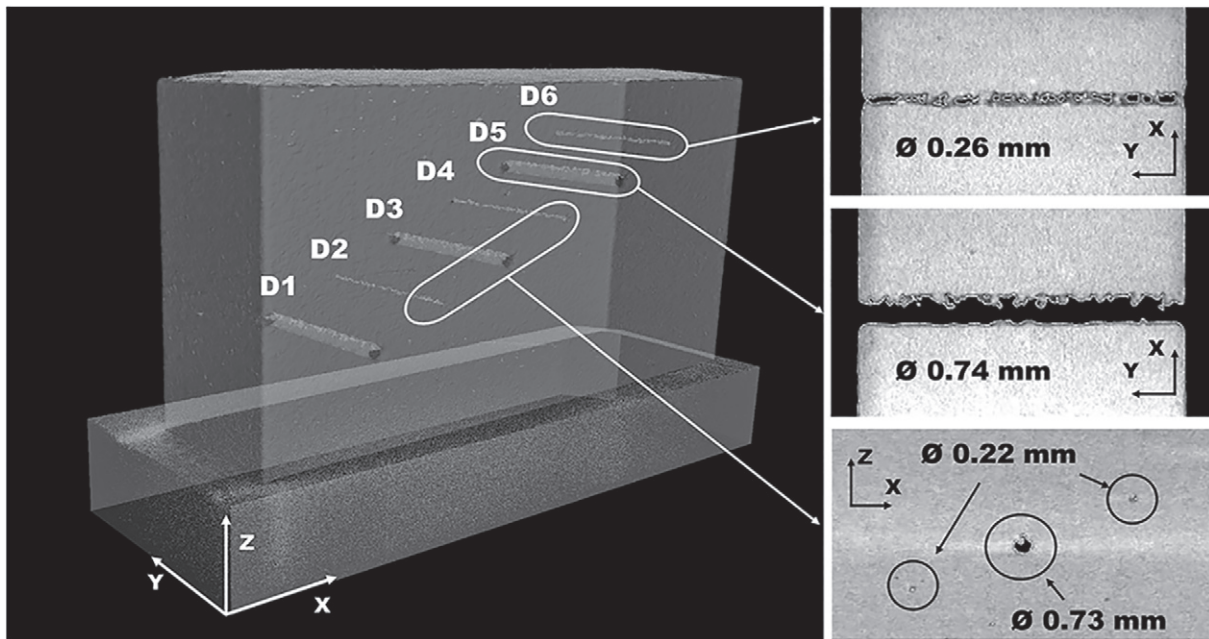

Fig. 7. 3D XCT data of the entire sample (left), with detailed horizontal cross-sections of D6 (top right) and D5 (center right) through holes and their measured diameters. D5 was clear along its length, with rough internal surfaces and a measured mean diameter of 0.74 mm. D6 had some back filling and a mean measured diameter of 0.26 mm. (bottom right) Cross-section of the holes and measured mean diameter.
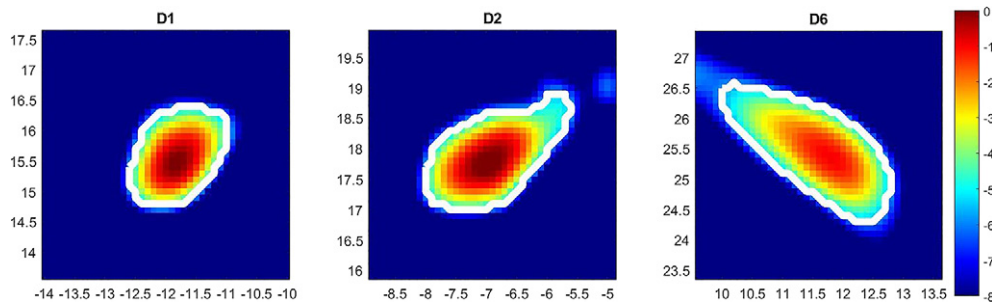
Fig. 9. Close-up TFM images of Fig. 5, showing mock side drilled holes: D1, D2 and D6. A 3 MHz digital filter was used for all figures and the dynamic range is shown (dB scale). The white outline shows the boundary of −6 dB drop in image pixels.

4.2. Sizing of features using LIPA

From Fig. 5 the features can be detected but sizing and characterization is difficult. This is because the ultrasonic wavelength of the shear wave at a frequency of 3 MHz is ~1 mm, which is close to the diffraction limit (0.5λ) making it impossible to size and characterize the features present [39,40], especially those with diameter of 0.2 mm. Fig. 9 shows a close up of features D1, D2 and D6, imaged at the 3 MHz frequency component of the shear wave. The line around the features shows the image pixels within −6 dB of the maximum pixel value of the indication. The diameter of indications are measured as the major axis of the best fit ellipse and are 2 mm for D1 (⌀ 0.7 mm), 2.8 mm for D2 (⌀ 0.2 mm) and 3.4 mm for D6 (⌀ 0.2 mm). As expected, using this frequency component it is not possible to size these features. It is noted here that sizing and characterization of the features requires further processing of the data set, e.g by comparing the predicted and experimentally measured scattering coefficient matrix [41]. However, such data processing is beyond the scope of the present paper.

4.3. Correlation of LIPA indications to XCT data

It is important to understand if the AM platform being used is producing components that meet the geometrical accuracy required for the parts being manufactured. There are a range of NDE techniques capable of measuring this post-manufacture but none that have the capability to locate nested features on-line. The through hole locations measured using XCT were overlaid on the LIPA indications and illustrated in Fig. 5. The black circles in Fig. 5 were plotted using the centroid of the indications from the LIPA data. The area of the plotted circles were proportional to the total area of the indication. The shallowest feature D1 at 16 mm was used as a starting point to anchor the measurements obtained from XCT, the white cross hairs were plotted where the XCT showed the center to be and the white circle represented the area based on the XCT measured diameter. Based on Table 1 the LIPA indications had a standard deviation of 0.34 mm in the X and 0.33 mm in the Z compared to the XCT data. The lack of a positive identification from D5 is due to being located at a region of low sensitivity of the shear wave and the internal roughness as discussed in Section 4.1. Although an indication was observed in the region where D5 was expected to be, the size and amplitude of it

was the same as the noise in that region. The indications D3 and D4 as seen in Fig. 6 were also located in the region of low sensitivity due to the angular dependency of the shear wave. This, combined with the internal roughness seen in AM, explains the larger indication and noise surrounding them. D6 showed the least variation in X and Z position compared to the XCT data, it was located in the region illustrated in Fig. 6, as the most efficient region for the generation and detection of shear waves using LIPA. This illustrated the best potential of LIPA to image features within AM components.

To improve the overall sensitivity of a LIPA inspection on a sample of this nature, the following can be implemented. A wider array with more elements would increase the region of high sensitivity and minimize the size of the blind spot, however it would increase the overall inspection time which using the existing setup was close to 3 h. Furthermore, the use of other ultrasonic wave modes for TFM imaging such as shear-longitudinal would also improve the sensitivity around 0°[31]. However, analysis of the captured LIPA signals using this mode did not produce good results, mainly due to the low SNR which made this low generation efficiency mode converted wave impossible to detect. The use of a higher power detection laser would increase the energy incident on the detector, thereby increasing the SNR and decreasing the number of averages required [42]. This would have a knock-on effect of decreasing the time taken for the inspection. For example, for an ultrasonic generation laser with 10 kHz repetition rate ($L_{rep.rate}$) - as opposed to our current 5 kHz laser - and a rough surface detection laser with 500 mW power returning to the detector -as opposed to the current >1 mW laser - would reduce the number of required averages (m_{aver}) to 20 - as opposed to currently 500 averages- and would reduce the theoretical limit for the data acquisition time (t_{FMC}) of a 129 element LIPA (N_{elem}) down to 33 s, as $t_{FMC} = (N_{elem})^2 m_{aver}(1/L_{rep.rate})$ [9]. In practice further overheads are expected due to the oscilloscope and mechanical scanning, however such system would require a few minutes to acquire data and would be fast enough for on-line inspection of AM. In addition, increasing SNR would improve multi-mode and multi-frequency analysis of the LIPA signals. Multi-mode analysis would allow TFM imaging using mode converted waves whilst multi-frequency analysis would allow imaging at higher ultrasonic frequency components, resulting in better-resolved features and increasing the probability of detection of the overall LIPA system [9].

5. Conclusion

This paper has successfully demonstrated the remote, couplant free, non-destructive inspection of an AM component off-line. This was accomplished by synthesizing LIPA on the underside of the AM component, using a simple experimental setup, adapting the FMC data acquisition and the TFM imaging algorithm to LU. The AM component included nested features as part of its design. The

Table 1
Offset in mm of LIPA indications compared to XCT position of features.

Indication	Δ X (mm)	Δ Z (mm)
D1	0	0
D2	0.08	0.49
D3	0.15	0.34
D4	0.30	0.94
D6	0.07	0.17

features had characteristics typical of AM, such as back filling and internal surface roughness, confirmed using XCT. This demonstrated the capability of LIPA to detect AM cylindrical features with internal roughness, as small as 0.2 mm in diameter, in a non-contact manner, providing 2-D, cross-sectional ultrasonic images. The features were detected using shear waves of 3 MHz frequency, giving an effective wavelength of 1 mm in aluminum. For this reason, sizing and characterization of the features was not possible although it could be achieved using further processing of the data [41]. A 1-D LIPA of 129 elements was synthesized, paving the way for 2-D LIPA that would be able to provide 3-D, volumetric inspection of AM. This type of 2-D array would be best suited for detecting spherical defects or voids resulting from the AM process and work is underway to address such cases. The features imaged in the present study were air-filled holes and the absence of unfused powder was verified from the XCT data. Typical AM defects can include powder-filled cavities which would affect the ultrasonic contrast of the imaged features and the effectiveness of the technique would need to be investigated in this case.

The LIPA presented here were synthesized on the under side of the build plate, which presented the advantage of controlling the sample surface and access related inspection parameters. This configuration could be useful for on-line process monitoring of relatively small AM components, of simple geometry and no overhanging features.

Future work in this area involves fabrication of components that are not directly coupled to the build plate but instead held using support structures. Furthermore, a systematic study on features of progressively smaller size from 0.5 mm to 0.1 mm is underway and will help to a) asses the detectability of spherical and other geometrical defects, b) gain an understanding of the system's minimum defect size detectability and c) form a good platform for future developments in this area, progressively varying the investigation into internal features that represent typical AM defects such as voids both empty and filled with powder and of various geometry.

For larger components with more complex geometries, LIPA would require to be synthesized on the build side of the component. This would require coping with the high temperatures of the AM process and the surface roughness of the components being built. Very few researchers have previously published on the effect of thermal gradients on ultrasonic phased array measurements: Marvasti and Sinclair [43] and Tezuka et al. [44] have done initial studies in this area, whilst the work by Patel et al. [21] shows the challenges faced by laser ultrasonic inspection of as-deposited, rough surfaced AM components. These are the current challenges for the technique introduced in this study and they are being addressed in our ongoing work.

Faster data acquisition for LIPA can be achieved by the use of higher repetition rate generation laser and higher power detection laser, reducing the time required per point, making the technique suitable for on-line process monitoring. In particular, increasing the power of the detection laser would increase SNR, allowing for multi-mode and multi-frequency analysis. The first would assist in detecting features which currently lie on sensitivity "blind spots" and the second would increase the detectability of features with sizes <100 μm, making the technique capable to detect defects found in PBF components.

Declaration of competing interest

The authors declare that they have no known competing financial interests or personal relationships that could have appeared to influence the work reported in this paper.

CRediT authorship contribution statement

Don Pieris: Writing - original draft, Writing - review & editing, Investigation, Conceptualization. **Theodosia Stratoudaki:** Investigation, Formal analysis, Software, Writing - original draft. **Yashar Javadi:** Investigation, Writing - original draft. **Peter Lukacs:** Investigation, Writing - original draft. **Sam Catchpole-Smith:** Methodology, Writing - original draft. **Paul D. Wilcox:** Software. **Adam Clare:** Conceptualization, Resources. **Matt Clark:** Conceptualization, Resources.

Acknowledgments

References

[1] ASTM International, F2792-12a - standard terminology for additive manufacturing technologies, Rapid Manufacturing Association, 2013, pp. 10–12. arXiv:1011.1669v3. http://www.ciri.org.nz/nzrma/technologies.html. https://doi.org/10.1520/F2792-12A.2.

[2] B.P. Conner, G.P. Manogharan, A.N. Martof, L.M. Rodomsky, C.M. Rodomsky, D.C. Jordan, J.W. Limperos, Making sense of 3-D printing: creating a map of additive manufacturing products and services, Addit. Manuf. 1 (2014) 64–76. https://doi.org/10.1016/j.addma.2014.08.005.

[3] M. Hirsch, P. Dryburgh, S. Catchpole-Smith, R. Patel, L. Parry, S.D. Sharples, I.A. Ashcroft, A.T. Clare, Targeted rework strategies for powder bed additive manufacture, Addit. Manuf. 19 (2018) 127–133. (November). https://doi.org/10.1016/j.addma.2017.11.011.

[4] M. Grasso, B.M. Colosimo, Process defects and *in situ* monitoring methods in metal powder bed fusion: a review, Meas. Sci. Technol. 28 (4) (2017) 044005. http://stacks.iop.org/0957-0233/28/i=4/a=044005?key=crossref.a2f14dcbe11fc719b4da4bf0797ef2dc. https://doi.org/10.1088/1361-6501/aa5c4f.

[5] M. Froend, V. Ventzke, S. Riekehr, N. Kashaev, B. Klusemann, J. Enz, Microstructure and microhardness of wire-based laser metal deposited AA5087 using an ytterbium fibre laser, Materials Characterization, vol. 143, Elsevier. 2018, pp. 59–67. https://doi.org/10.1016/j.matchar.2018.05.022.

[6] S. Berumen, F. Bechmann, S. Lindner, J.-P. Kruth, T. Craeghs, Quality control of laser- and powder bed-based additive manufacturing (AM) technologies, Phys. Procedia 5 (2010) 617–622. https://doi.org/10.1016/j.phpro.2010.08.089.

[7] M. Doubenskaia, M. Pavlov, S. Grigoriev, E. Tikhonova, I. Smurov, Comprehensive optical monitoring of selective laser melting, J. Laser Micro/Nanoeng. 7 (3) (2012) 236–243. http://www.scopus.com/inward/record.url?eid=2-s2.0-84869801432&partnerID=40&md5=2d50074f42c444460de4e4599ee8f29e. https://doi.org/10.2961/jlmn.2012.03.001.

[8] J.A. Kanko, A.P. Sibley, J.M. Fraser, In situ morphology-based defect detection of selective laser melting through inline coherent imaging, J. Mater. Process. Technol. 231 (2016) 488–500. https://doi.org/10.1016/j.jmatprotec.2015.12.024.

[9] T. Stratoudaki, M. Clark, P.D.P. Wilcox, Y. Javadi, W. Kerr, P.D.P. Wilcox, D. Pieris, M. Clark, Laser induced ultrasonic phased array using full matrix capture data acquisition and total focusing, Opt. Express 24 (19) (2016) 21921–21938. https://www.osapublishing.org/abstract.cfm?URI=oe-24-19-21921. https://doi.org/10.1364/OE.24.021921.

[10] A. Thompson, I. Maskery, R.K. Leach, X-ray computed tomography for additive manufacturing: a review, Meas. Sci. Technol. 27 (7) (2016) 72001. https://doi.org/10.1088/0957-0233/27/7/072001.

[11] H. Villarraga-Gómez, C.M. Peitsch, A. Ramsey, S.T. Smith, The role of computed tomography in additive manufacturing, Proceedings - 2018 ASPE and euspen Summer Topical Meeting: Advancing Precision in Additive Manufacturing, 2018, pp. 201–210. (July).

[12] F.H. Kim, H. Villarraga-Gómez, S.P. Moylan, Inspection of embedded internal features in additively manufactured metal parts using metrological X-ray computed tomography, Proceedings - ASPE/euspen 2016 Summer Topical Meeting: Dimensional Accuracy and Surface Finish in Additive Manufacturing, 2016, pp. 191–195.

[13] J. Mireles, S. Ridwan, P.A. Morton, A. Hinojos, R.B. Wicker, Analysis and correction of defects within parts fabricated using powder bed fusion technology, Surf. Topogr. Metrol. Prop. 3 (3). (2015) https://doi.org/10.1088/2051-672X/3/3/034002.

[14] A.A. Martin, N.P. Calta, J.A. Hammons, S.A. Khairallah, M.H. Nielsen, R.M. Shuttlesworth, N. Sinclair, M.J. Matthews, J.R. Jeffries, T.M. Willey, J.R. Lee, Ultrafast dynamics of laser-metal interactions in additive manufacturing alloys captured by in situ X-ray imaging, Mater. Today Adv. 1 (2019) 100002. https://doi.org/10.1016/j.mtadv.2019.01.001.

[15] A. Du Plessis, I. Yadroitsev, I. Yadroitsava, S.G. Le Roux, X-ray microcomputed tomography in additive manufacturing: a review of the current technology and applications, 3D Printing and Additive Manufacturing, 5, 2018, pp. 227–247. (3). https://doi.org/10.1089/3dp.2018.0060.

[16] H. Rieder, A. Dillhöfer, M. Spies, J. Bamberg, T. Hess, Online monitoring of additive manufacturing processes using ultrasound, Proceedings of the 11th European Conference on Non-Destructive Testing, 1, 2014, pp. 2194–2201. (Ecndt).

[17] H. Rieder, M. Spies, J. Bamberg, B. Henkel, On- and offline ultrasonic inspection of additively manufactured components, 19th World Conference on Non-Destructive Testing 2016, 2016, pp. 1–8.

[18] Y. Javadi, C.N. Macleod, S.G. Pierce, A. Gachagan, W. Kerr, J. Ding, S. Williams, M. Vasilev, R. Su, C. Mineo, J. Dziewierz, Ultrasonic phased array inspection of wire + arc additive manufacture samples using conventional and total focusing method imaging approaches, Insight - Non-Destr. Test. Cond. Monit. 61 (2) (2019) 144–148.

[19] L.-S. Wang, J.S. Steckenrider, J.D. Achenbach, A fiber-based laser ultrasonic system for remote inspection of limited access components, Tech. Rep., 2013, Boston, MA. https://doi.org/10.1007/978-1-4615-5947-4_67.

[20] M. Dubois, M. Militzer, A. Moreau, J.F. Bussière, A new technique for the quantitative real-time monitoring of austenite grain growth in steel, Scr. Mater. 42 (9) (2000) 867–874. http://linkinghub.elsevier.com/retrieve/pii/S1359646200003055. https://doi.org/10.1016/S1359-6462(00)00305-5.

[21] R. Patel, M. Hirsch, P. Dryburgh, D. Pieris, S. Achamfuo-Yeboah, R. Smith, R. Light, S. Sharples, A. Clare, M. Clark, Imaging material texture of as-deposited selective laser melted parts using spatially resolved acoustic spectroscopy, Appl. Sci. 8 (10) (2018) 1991. http://www.mdpi.com/2076-3417/8/10/1991. https://doi.org/10.3390/app8101991.

[22] S. Everton, P. Dickens, C. Tuck, B. Dutton, Using laser ultrasound to detect subsurface defects in metal laser powder bed fusion components, Jom (2017) 1–6. https://doi.org/10.1007/s11837-017-2661-7.

[23] D. Lévesque, C. Bescond, M. Lord, X. Cao, P. Wanjara, J.P. Monchalin, Inspection of additive manufactured parts using laser ultrasonics, AIP Conf. Proc. 1706 (2016) (July 2018). https://doi.org/10.1063/1.4940606.

[24] R.J. Smith, M. Hirsch, R. Patel, W. Li, A.T. Clare, S.D. Sharples, Spatially resolved acoustic spectroscopy for selective laser melting, J. Mater. Process. Technol. 236 (2016) 93–102. https://doi.org/10.1016/j.jmatprotec.2016.05.005.

[25] M. Hirsch, R. Patel, W. Li, G. Guan, R.K. Leach, S.D. Sharples, A.T. Clare, Assessing the capability of in-situ nondestructive analysis during layer based additive manufacture, Addit. Manuf. 13 (2017) 135–142. https://doi.org/10.1016/j.addma.2016.10.004.

[26] A.J.A. Bruinsma, J.A. Vogel, Ultrasonic noncontact inspection system with optical fiber methods, Appl. Opt. 27 (22) (1988) 4690. https://doi.org/10.1364/ao.27.004690.

[27] C. Fan, M. Caleap, M. Pan, B.W. Drinkwater, A comparison between ultrasonic array beamforming and super resolution imaging algorithms for non-destructive evaluation, Ultrasonics 54 (7) (2014) 1842–1850. https://doi.org/10.1016/j.ultras.2013.12.012.

[28] C. Holmes, B.W. Drinkwater, P.D. Wilcox, Post-processing of the full matrix of ultrasonic transmit receive array data for non-destructive evaluation, NDT & E Int. 38 (2005) 701–711. https://doi.org/10.1016/j.ndteint.2005.04.002.

[29] C.B. Scruby, L. Drain, Laser Ultrasonics, Adam Hilger, Bristo, 1990.

[30] L.R.F. Rose, Point-source representation for laser-generated ultrasound, J. Acoust. Soc. Am. (2005) https://doi.org/10.1121/1.390583.

[31] T. Stratoudaki, M. Clark, P.D. Wilcox, Adapting the full matrix capture and the total focusing method to laser ultrasonics for remote non destructive testing, IEEE Int. Ultrason. Symp., IUS (2017) 3–6. https://doi.org/10.1109/ULTSYM.2017.8092864.

[32] G.W. Kaye, T.H. Laby, Tables of physical and chemical constants, Z. Kristallogr. - New Cryst. Struct. 212 (5) (1997) 400. https://doi.org/10.1524/zkri.1997.212.5.400.

[33] S.-c. Wooh, Y. Shi, Optimum beam steering of linear phased arrays, 29. 1999, 245–265.

[34] G. Huang, Z. Min, L. Yang, P.X. Jiang, M. Chyu, Transpiration cooling for additive manufactured porous plates with partition walls, Int. J. Heat Mass Transf. 124 (2018) 1076–1087. https://doi.org/10.1016/j.ijheatmasstransfer.2018.03.110.

[35] N.T. Aboulkhair, N.M. Everitt, I. Ashcroft, C. Tuck, Reducing porosity in AlSi10Mg parts processed by selective laser melting, Addit. Manuf. 1 (2014) 77–86. https://doi.org/10.1016/j.addma.2014.08.001.

[36] J.P. Monchalin, J.D. Aussel, R. Héon, C.K. Jen, A. Boudreault, R. Bernier, Measurement of in-plane and out-of-plane ultrasonic displacements by optical heterodyne interferometry, J. Nondestruct. Eval. 8 (2) (1989) 121–133. https://doi.org/10.1007/BF00565636.

[37] P. Delaye, A. Blouin, L.-A. de Montmorillon, D. Drolet, G. Roosen, J.-P. Monchalin, L.-A. de Montmorillon, G. Roosen, J.-P. Monchalin, Detection of ultrasonic motion of a scattering surface by photorefractive InP:Fe under an applied dc field, J. Opt. Soc. Am. B 14 (7) (1997) 1723–1734. http://josab.osa.org/abstract.cfm?URI=josab-14-7-1723. https://doi.org/10.1364/josab.14.001723.

[38] A. McGilp, J. Dziewierz, T. Lardner, J. Mackersie, A. Gachagan, Inspection design using 2D phased array, TFM and cueMAP software, AIP Conference Proceedings, vol. 1581 33, 2014, pp. 65–71. https://doi.org/10.1063/1.4864803.

[39] J. Zhang, B.W. Drinkwater, P.D. Wilcox, The use of ultrasonic arrays to characterize crack-like defects, J. Nondestruct. Eval. 29 (4) (2010) 222–232. https://doi.org/10.1007/s10921-010-0080-6.

[40] A.A. Maznev, O.B. Wright, Upholding the diffraction limit in the focusing of light and sound, Wave Motion 68 (2017) 182–189. arXiv: 1602.07958. https://doi.org/10.1016/j.wavemoti.2016.09.012.

[41] J. Zhang, B.W. Drinkwater, P.D. Wilcox, Defect characterization using an ultrasonic array to measure the scattering coefficient matrix, IEEE IEEE Trans. Ultrason. Ferroelectr. Freq. Control 55 (10) (2008) 2254–2265. https://doi.org/10.1109/TUFFC.924.

[42] J.-P. Monchalin, Monchalin, Progress towards the application of laser-ultrasonics in industry, Review of Progress in Quantitative Nondestructive Evaluation, 12, 1993, pp. 495–506. file:/ce/rd\protect\T1\textbraceleft_\protect\T1\textbracerightorganisation/PTA-MAD/Common/10Literature/2008/Properties/Techniques/laserultrasonics/Monchalin(1993)#Progresstowardstheapplicationoflaser-ultrasonicsinindustry.pdf. https://doi.org/10.1007/978-1-4615-2848-7_64.

[43] M.H. Marvasti, A.N. Sinclair, Phased array inspection at elevated temperatures, 2014, pp. 854–857. https://doi.org/10.1109/ULTSYM.2014.0210.

[44] K. Tezuka, M. Mori, S. Wada, M. Aritomi, H. Kikura, Y. Sakai, Analysis of ultrasound propagation in high-temperature nuclear reactor feedwater to investigate a clamp-on ultrasonic pulse Doppler flowmeter, J. Nucl. Sci. Technol. 45 (2008) 752–762. https://doi.org/10.3327/jnst.45.752.